
REMOTE SENSING OF ATMOSPHERE,
HYDROSPHERE, AND UNDERLYING SURFACE

Observations of Meteoric Aerosol in the Upper Stratosphere–Lower Mesosphere by the Method of Two-Wavelength Lidar Sensing

V. A. Korshunov^{a,*}, E. G. Merzlyakov^{a,**}, and A. A. Yudakov^{a,***}

^aTaifun Scientific Production Association, Kaluga oblast, Obninsk, 249038 Russia

*e-mail: korshunov@rpatyphoon.ru

**e-mail: eugmer@rpatyphoon.ru

***e-mail: yudakov@rpatyphoon.ru

Received May 24, 2018; revised July 25, 2018; accepted August 18, 2018

Abstract—We present the results of two-wavelength lidar sensing of the middle atmosphere in the altitude range from 30 to 60 km over Obninsk (55.1° N, 36.6° E) in 2012–2017. Monthly average values of the ratio of aerosol and Rayleigh backscattering coefficients (RARC) at a wavelength of 532 nm, averaged over the layers of 40–50 km and 50–60 km, vary from 0 to 0.02, while the average peak RARC levels in these layers vary from 0.1 to 0.2. Short-term (shorter than 1 month) and long-term (half-year and longer) variations in backscattering are observed. Short-term variations are time concurrent with the occurrence of meteor showers. Long-term enhancements of backscattering in the layer of 50–60 km were observed in 2013 after the Chelyabinsk meteorite fall, as well as in the first half of 2016. In 2014–2015, the monthly average RARC was zero within measurement errors at altitudes from 40 to 60 km. We analyzed the possibility for meteoric aerosol to manifest in backscattering, taking into account the fluxes of meteoric material, gravitational sedimentation of aerosol, and the effect of vertical wind. The flux of visible meteors with masses larger than 10^{-6} kg and bolides is shown to be insufficient for a long-term enhancement of backscattering in the layer of 50–60 km. It is hypothesized that the enhancement in backscattering is most likely to be due to the occurrence of an enlarged fraction of meteoric smoke particles, formed by ablation of radio meteors and penetrating into the upper stratosphere in the region of the stratospheric polar vortex. In early 2016, this was favored by the formation of an extremely strong stratospheric polar vortex and its shift toward Eurasia.

Keywords: lidar, backscattering, middle atmosphere, meteoric aerosol, meteoric smoke

DOI: 10.1134/S1024856019010081

INTRODUCTION

Experimental studies of aerosol in the middle atmosphere have been performed by different methods for quite a long time [1]. However, the information on aerosol is still very poor because both the studies themselves and their interpretation are beset by large difficulties [2]. Aerosol in the middle atmosphere is also studied through simulation, incorporating the processes of aerosol formation, transformation, and transport in the atmosphere. In particular, models of meteoric smoke are developed, envisaging that meteoroids hundreds of microns in size are ablated at altitudes of 75–120 km to form nanometer-sized particles which, entrained by air in the system of atmospheric general circulation, are then carried to the upper stratosphere [3]. Nanometer-sized aerosol is invisible in scattering and, in particular, in lidar and satellite measurements; however, it can be recorded in absorption on long atmospheric paths in satellite measurements of extinction. It is thought that the data from Solar Occultation For Ice Experiment (SOFIE) onboard the Aeronomy of Ice in the Mesosphere (AIM)

platform largely confirm the meteoric smoke model predictions [4, 5].

At the same time, there are data from lidar observations [6–8] and other optical measurements [9], in which aerosol in the middle atmosphere is manifested in scattering, contrary to what is expected from the existing meteoric smoke models. The lidar measurements of aerosol layers are often explained by the occurrence of spontaneous meteoric traces, not contributing sensibly to the total aerosol loading of the middle atmosphere [10]. Formation of particles in the submicron size range in traces of large bolides is demonstrated in lidar measurements [11, 12]. There were also other explanations for the occurrence of aerosols in the middle atmosphere. For instance, the authors of [13] resorted to considerations about levitation of micron-sized aerosol particles and a certain structure as a result of the gravitophoresis phenomenon. The authors of work [14] proposed that a dynamically stable aerosol layer in the stratosphere can be formed under the influence of a vertical wind entraining particles. The authors of work [7] argued

that an interrelation exists between the precipitation of high-energy electrons in the middle atmosphere of Kamchatka and the occurrence of layers with enhanced aerosol scattering at altitudes of 60–75 km. By itself, the presence of submicron and micron particles in the upper stratosphere is also confirmed by in situ sampling of aerosol substances [15].

The discussion above indicates that our knowledge of aerosol in the middle atmosphere is incomplete and controversial, to some degree, warranting further study. In this work, we present the results of two-wavelength lidar sensing of the middle atmosphere. In contrast to one-wavelength sensing, our method makes it possible, within certain a priori assumptions on aerosol microphysics, to distinguish between the contributions from temperature fluctuations and the aerosol component to the signal observed. Lidar measurements are analyzed and compared to other known data on aerosol in the middle atmosphere.

The lidar measurements were performed using an AK-3 lidar developed at the Taifun Scientific Production Association, Obninsk. At present, the AK-3 lidar is operated at seven remote sensing stations on the territory of the Russian Federation. Most measurements, since 2012 with a 0.5-year suspension in 2013, were performed at the base station in Obninsk. Episodic measurements were also performed at other stations. In the present work, we use the measurements from Obninsk and Ardon (Republic of North Ossetia, Alania).

TECHNIQUE FOR MEASUREMENTS AND DATA PROCESSING

Lidar measurements are usually used to calculate the backscattering ratio $R = (\beta_a + \beta_R)/\beta_R$, where β_a and β_R are the aerosol and Rayleigh backscattering coefficients. In two-wavelength measurements, the altitudinal profile $R(532, h)$ at a wavelength of 532 nm (h is the altitude) is determined from the calibrated difference of the logarithms of signals $\Delta(h) = [\ln F(355, h) - \ln F(532, h)] + K$:

$$R(532, h) = (1 - C)/[\exp(\Delta(h)) - C], \quad (1)$$

where K is the calibration constant; and the parameter C depends on the ratio of aerosol backscattering coefficients at the sensing wavelength and is set a priori to 0.23 [8]. The quantity $R(532, h) - 1 = \beta_a(532)/\beta_R(532)$ characterizes the relative aerosol content in the atmosphere. The results of the $R(532, h) - 1$ measurements are presented in the altitude range from 30 to 65 km.

The $\Delta(h)$ calibration was performed according to the maximum of $\Delta(h)$ in the altitude range from 26 to 48 km, where at the point of maximum it was assumed that $\Delta(h)_{\max} = 0$ and the constant K was determined [8]. To eliminate the noise bias in $\Delta(h)_{\max}$, in the found value $\Delta(h)_{\max}$ we introduced a correction that depends on the noise level in a given specific measurement. The statistically averaged correction as a function of

the noise level was determined in numerical experiments beforehand. A characteristic value of the correction was within the range $|\Delta(h)| < 0.01$. In some respects, this method is similar to the calibration method in one-wavelength sensing, when signal referencing is carried out at the point of the signal minimum. In contrast, in our case the variations in the atmospheric density do not influence the calibration.

Sensing was performed in the vertical direction. Backscattered signals at wavelengths of 355 and 532 nm were recorded by the photon counting method. The overburden of receivers in the near-field zone was avoided using mechanical cut-off of this zone to a range of 21 km. Gate length in recording was 150 m, in distance units. Typical accumulation time in a single session was 1 h. During signal processing in our work we carried out current signal averaging within a distance of 1 km, which precisely determined the spatial resolution of the results.

The $R(532, h) - 1$ values are generally very small in the middle atmosphere; therefore, we carefully examined the noise component of signals and its influence on the measurements. As is well known, the measurement errors in the photon counting mode are determined by statistical noise in recording the photoelectrons, described by the Poisson distribution [16]. To check how the actual parameters of photo recording agree with theoretical estimates, experiments were performed with recording the distribution of photo counts from a thermal source. For this, radiation from a stabilized filament lamp was directed to the entrance of receiving telescope. The recording parameters were selected so as to be close to those in atmospheric measurements; for this, signals at 355 and 532 nm were equated using additional filters. It is noteworthy that the number of photo electrons accumulated in a single experiment was quite large, so that the Poisson distribution was well fitted to a normal distribution [16]. We considered the spectrum of fluctuations in the difference between logarithms of signals at wavelengths of 355 and 532 nm:

$$\Delta(n) = [\ln F(n, 532) - \langle \ln F(n, 532) \rangle] - [\ln F(n, 355) - \langle \ln F(n, 355) \rangle], \quad (3)$$

where n is the gate number in the signal record, and averaging ($\langle \rangle$) was over all gates.

The theory dictates that $\Delta(n)$ should be normally distributed with the variance $\sigma_y^2 = 1/N_{532} + 1/N_{355}$, where N_{532} and N_{355} are the average numbers of photo counts in a single time gate. Skipping the details of analysis of the measured $\Delta(n)$ distributions, we note that theoretical and experimental distributions coincided within the errors. It is important to note that the experimental $\Delta(n)$ distribution was symmetric about zero.

One of the error sources in lidar measurements may be the dependence of Rayleigh scattering cross section on the temperature when narrowband interference fil-

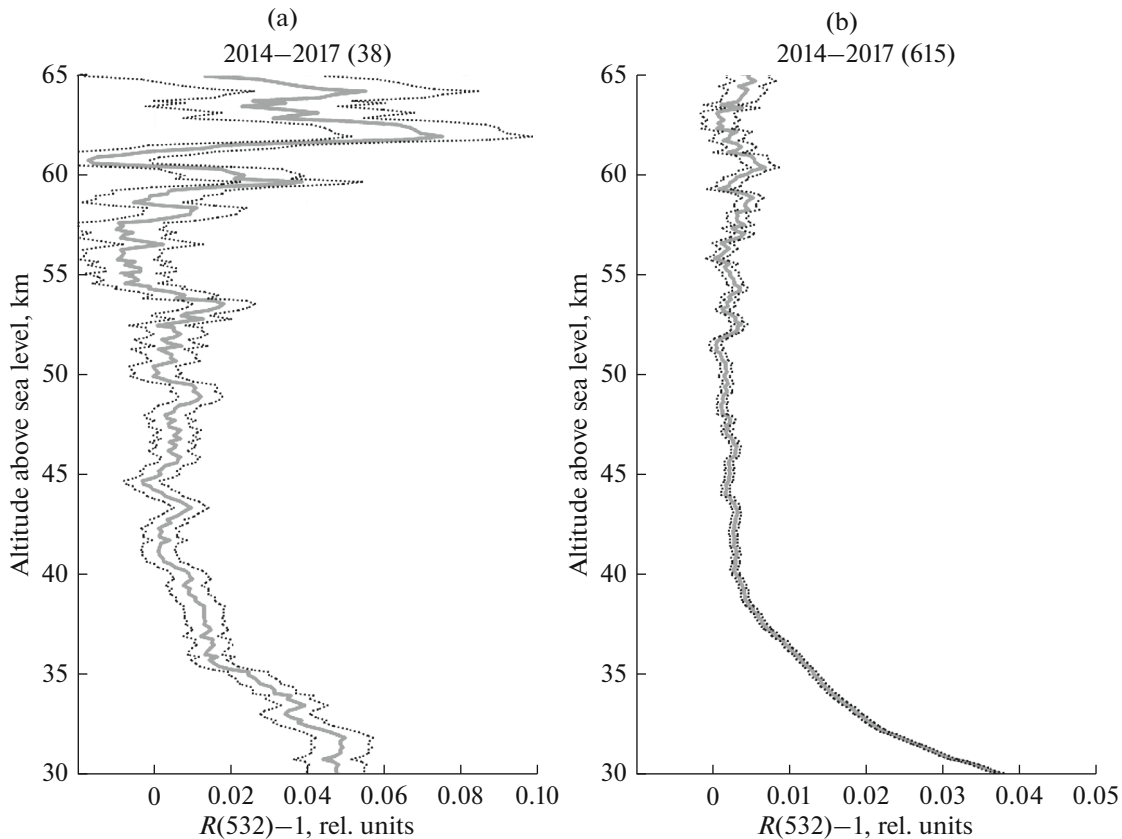


Fig. 1. Average altitudinal profiles of backscattering ratio $R(532, h)$ in (a) Ardon and (b) Obninsk for the entire period of measurements. Dotted lines indicate the statistical error corridor. Numbers of hourly measurements are given in parentheses.

ters are utilized, especially if the filter passband maximum is shifted relative to the spectral line of the sensing radiation [17]. The method in work [18] was used to estimate this effect for the set of parameters, characteristic for our measurements: mean calibration altitude is 40 km, atmospheric temperature in the altitude range of sensing varies by ± 20 K relative to the calibration altitude, full width at half-maximum of the interference filter passband is 2 nm, and a possible shift in the maximum of the filter passband is ± 1 nm. The results showed that the variations in Rayleigh scattering cross section do not exceed 0.12% for these parameters. An additional error source is the nonlinearity of the counting characteristic of photo recording. The calculated nonlinearity did not exceed 0.5% at altitudes higher than 40 km and decreased to the 0.15% level, taking into account the correction made. The general measurement error, non-statistical in origin, is estimated as 0.2%.

MEASUREMENT RESULTS

Figure 1 shows the altitude profiles of $R(532, h) - 1$, averaged over all the period of measurements in Obninsk in 2012–2017 (615 measurements) and Ardon in 2014–2017 (38 measurements). The profile mea-

sured in Obninsk shows that $R(532, h) - 1$ is nearly zero starting from the 40-km level and above, indicating that, on the average over all years of observations, backscattering at these altitudes was nearly Rayleigh-type. The $R(532, h) - 1$ profile determined from measurements in Ardon is based on fewer measurements and, as such, is noisier. Nonetheless, qualitatively, both profiles show similar $R(532, h) - 1$ variations with altitude, except at an altitude of 62 km over Ardon where there is a layer with $R(532, h) - 1 = 0.07$, i.e., nonzero at the 3σ level, where σ is the standard deviation. This feature of the profile is, most probably, because the layers occur at random, and because the sample for Ardon is much smaller.

Figure 2 shows time variations in the annual average $R(532, h) - 1$ profiles from 2012 to 2017 (during only first half-year, in 2013) in Obninsk; evidently, the altitude profiles of $R(532, h) - 1$ are more variable on a year-long scale. In particular, in 2014 and 2015, the $R(532, h) - 1$ values become Rayleigh-type with growing altitude, with minor variations. In other years, a certain increase in $R(532, h) - 1$ is observed to a varying degree, when approaching the altitude range 60–65 km. In 2013, thick aerosol structures from the Chelyabinsk meteorite were observed for about 20 days in late February to early March at altitudes from 34 to

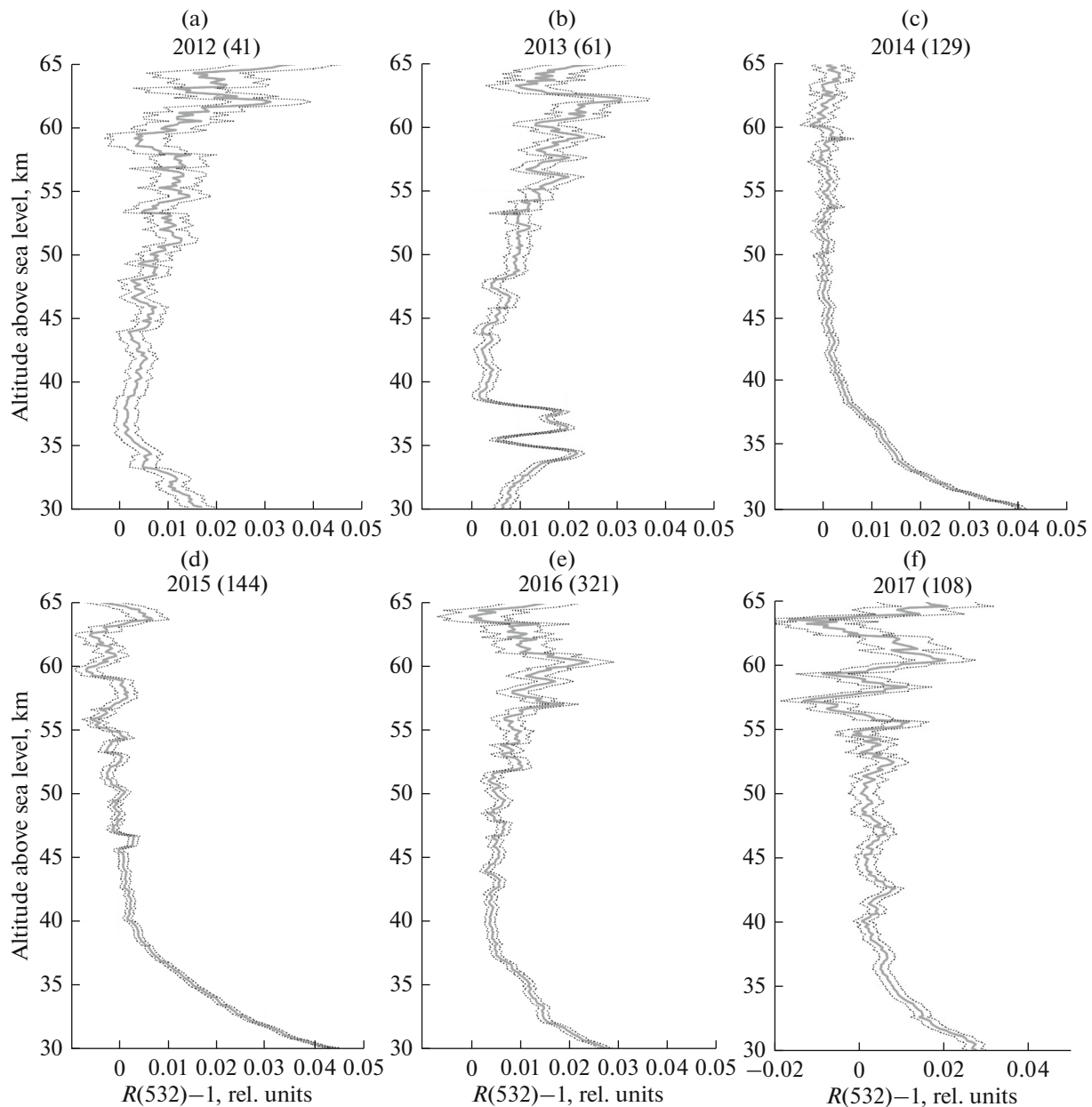


Fig. 2. Annual average profiles of backscattering ratios in Obninsk. The designations are the same as in Fig. 1.

37 km [12]. As can be seen from Fig. 2, traces of these structures survived even after 0.5-year averaging. In 2017, at high altitudes, the $R(532, h) - 1$ behavior is oscillatory in character, partly due to larger errors of measurements under less favorable atmospheric conditions.

Figure 3 shows the time behavior of monthly average $R(532) - 1$ values, averaged over the altitude layers 50–60, 40–50, and 35–40 km, with the indication of the statistical error corridor of the current average. From Fig. 3a it can be seen that $R(532) - 1$ significantly far from zero in the layer 50–60 km in 2012, 2013, and 2016. After the “quiescent” period 2014–

2015, there was an abrupt increase in $R(532) - 1$ in 2015, followed by a relaxation throughout 2016. Against the background of the decreasing $R(532) - 1$ average, we can discern a few secondary peaks in January, March, and June 2016. To characterize more carefully the $R(532) - 1$ behavior in the layer 50–60 km, Fig. 4 shows peak $R(532) - 1$ levels in this layer, exceeding the 2σ level. Dots indicate individual measurements, and solid lines show current averaging of monthly averages. As can be seen from Fig. 4, for the entire period of measurements, except the maximum in 2016, the peak levels were mostly around 0.1. They increased in late 2015; and in 2016 they were, on aver-

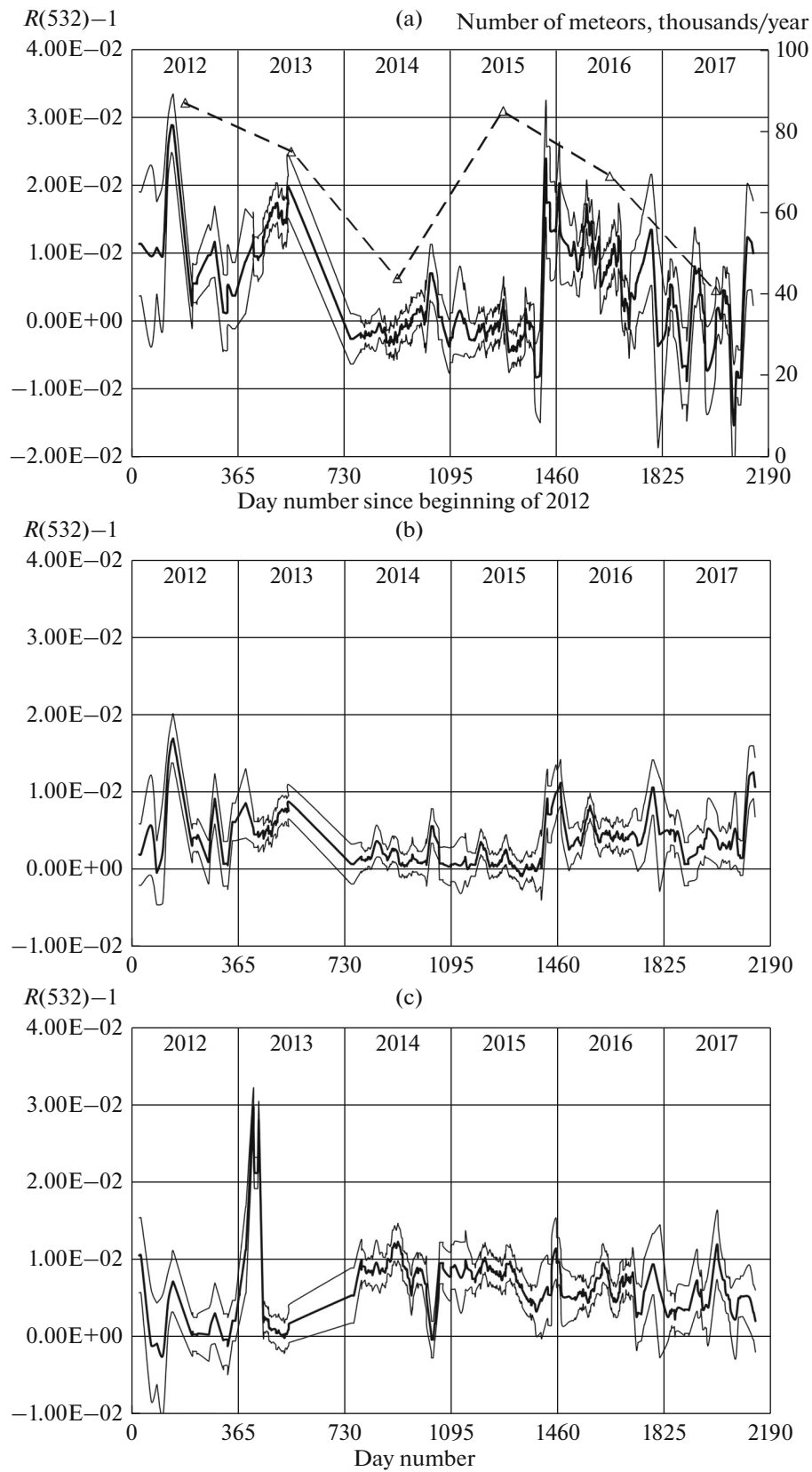


Fig. 3. Time behavior of monthly average $R(532) - 1$ (semi-thick line), averaged over (a) 50–60 km, (b) 40–50 km, and (c) 35–40 km layers. Dashed line in fragment (a) shows the number of visually observed meteors per year, based on the International Meteor Organization (IMO) data; thin lines show the statistical error corridor.

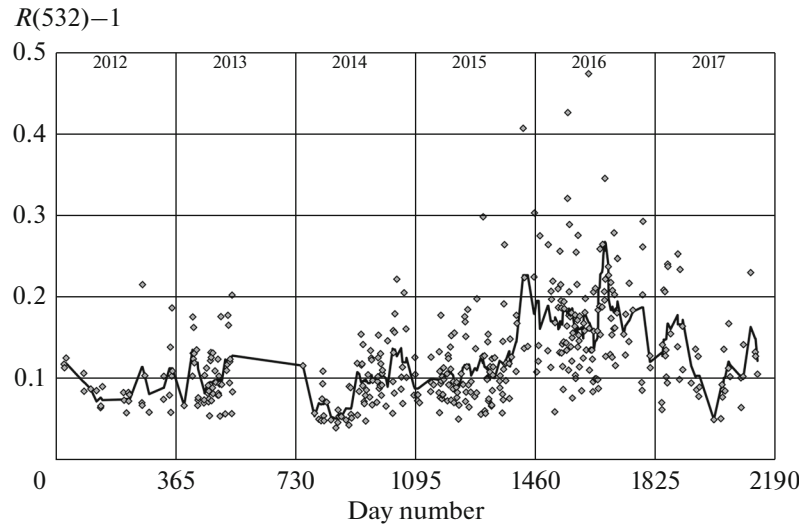


Fig. 4. Peak $R(532) - 1$ values in the layer 50–60 km. Dots indicate individual measurements, and line shows the monthly average value of current average.

age, around 0.2, sometimes attaining 0.5 and more (not shown in Fig. 4). The large difference between the peak and average levels is explained by the inhomogeneity of the altitudinal distribution of aerosol.

Oscillations in the 40–50 km layer (Fig. 3b) are similar to those in 50–60 km layer, but with a smaller amplitude. The $R(532) - 1$ variations in the layer 35–40 km (Fig. 3c) were in antiphase with higher layers: e.g., the $R(532) - 1$ level in 2014–2015 was higher than in 2016. The $R(532) - 1$ peak at 35–40 km in 2013 reflects the occurrence of a thick layer from the Chelyabinsk meteorite at altitudes of 34–37 km [12]. From Figs. 3a–3c it can be seen that, after the meteorite fall and until the end of measurements in 2013 (late June), $R(532, h)$ kept growing in layers 40–50 and 50–60 km; however, the $R(532) - 1$ decreased in the layer 35–40 km at that time.

We should note the time coincidence of enhanced-scattering episodes recorded by us and the occurrence of well-known meteor showers. For instance, the 2012 May peak (Fig. 3a) is time coincident with Eta Aquarid Meteor Shower. In the 40–50 km layer (Fig. 3b) an abrupt $R(532, h) - 1$ increase is regularly observed in October–November, when the South and North Tau-

rids become maximally active. Though not belonging to the maximally active, these showers contain an elevated number of large meteors [19]. Taurids might have contributed appreciably to increased aerosol content in the 50–60 km layer in 2015. It is well known that, as a result of the 7 : 2 resonance with Jupiter, the Taurids shower periodically intensifies, and the last Taurids peak was in 2015 [20].

The interannual variations, shown in Fig. 3a, can also be compared with data of visual observations of meteors, presented at the International Meteor Organization (IMO) website [21]. The number of observed meteors (in thousands per year) is shown in Fig. 3a by a dashed line. The time variations in visually observed episodes can be seen to qualitatively agree with lidar data in the 50–60 km layer, at least in terms of the 2014 and 2017 minima.

DISCUSSION OF RESULTS

The above-indicated measurements of altitude profiles of the backscattering ratio show that, averaged over a long-term period, $R(532, h) - 1$ values exceed the zero level by more than 0.02 in the altitude range

Table 1. Meteoric substance fluxes in different mass and size ranges

Meteoritic material	Size	Mass, kg	Flux, 10^3 t/yr
Micrometeors	10 ... 100 μm	10^{-12} ... 10^{-9}	3.0 [25]
Spherules	50 ... 700 μm	10^{-11} ... 3×10^{-8}	2.7 [2]
Radio meteors	10 ... 10^3 μm	10^{-12} ... 10^{-6}	1.4 ... 19 [24] 16 [3]
Visible meteors	1 ... 20 mm	10^{-6} ... 10^{-2}	0.13 [23]
Bolides	2 ... 200 cm	10^{-2} ... 10^4	0.41 [26]

from 40 to 60 km. Aerosol is predominately meteoric in origin in this altitude range. The $R(532, h) - 1$ value gradually increases below 40 km, primarily due to the formation of sulfate-meteoric aerosol [22].

Next, we will dwell on variations in aerosol content in the 40–50 and 50–60 km layers, which, in our opinion, are of the greatest interest. We will consider possible causes for the long-term $R(532) - 1$ growth in 2016, taking into account the existing statistically average data on meteoric material in the middle atmosphere. As is well known, the meteoric material, entering the atmosphere, has a wide meteoroid size (or mass) distribution [23]. Table 1 presents global meteor material fluxes in different meteoroid mass and size ranges based on the known literature data. Boundaries between the meteoroids of different types are quite arbitrary. The relationship between the mass and sizes in Table 1 corresponds to the density of 1.9 g/cm^3 . It should be kept in mind that the flux data, obtained by different authors and methods, may differ, sometimes very strongly [2, 24]. Table 1 presents certain averages over different sources.

From Table 1 it can be seen that the meteor material flux is maximal in the characteristic size range from 10 to $10^3 \mu\text{m}$. A certain particle fraction from this size range is subject to ablation at altitudes of 90–110 km with the formation of ionized traces, detected in radio radar measurements (radio meteors). The fraction of particles less than $100 \mu\text{m}$ in size, entering the atmosphere at relatively small velocities, is not ablated. These include micrometeors and spherules. Owing to their relatively large sizes, micrometeors and spherules quite rapidly sediment and are not manifested in scattering [2, 25].

The observed lidar signals can also be due to meteoric traces, i.e., the evaporated products of quite large meteoroids (fractions of centimeters and more in size), penetrating deep to the atmosphere. The altitude range where meteoric traces are formed is quite wide, spanning from 90 to 20 km [19, 27]. It is noteworthy that meteoroids of comet origin (and, in particular, Taurids), as well as relatively slow meteoroids originating from asteroids (and, in particular, Geminids), are fragmented at altitudes from 50 to 60 km [19].

We will estimate possible $R(532) - 1$ values in the 50–60 km layer, based on the known meteoric material fluxes and particle sedimentation velocity. The local flux $G [\text{g cm}^{-2} \text{s}^{-1}]$ will be specified assuming that the global meteoric material fluxes (see Table 1) are uniformly distributed in space over the Earth's surface and in time throughout the year. Particles with radii of tens of nanometers and larger may be manifested in the backscattered radiation. Gravitational sedimentation can play a significant role for particles with such sizes. The gravitational sedimentation rates V_{gravity} were calculated for spherical particles with a density of 1.9 g/cm^3 , using formulas presented in [14]. The characteristic V_{gravity} values were found to be 2.6, 5.9, and

26 mm/s for particles with radii of 0.046, 0.10, and $0.46 \mu\text{m}$. The V_{gravity} values will be two times smaller for porous particles with the density $\rho \sim 1 \text{ g/cm}^3$, which can be present in meteoric aerosol composition [28, 29].

The ERA5 data, i.e., the fifth generation of the European Centre for Medium-Range Weather Forecasts (ECMWF) atmospheric reanalyses of the global climate, will be used to estimate the effect of vertical wind on particle sedimentation rate. The zonal mean vertical wind was calculated taking into account quite a slow sedimentation of submicron aerosol in the region 50–60 km. This was done using ERA5 data on the vertical wind at 137 model levels; these were obtained by ensemble averaging with the 3-h resolution in time. We carried out sampling of data on vertical speeds dp/dt (p is the pressure, speed is in units of Pa/s) for the latitudinal belt $55\text{--}56^\circ \text{ N}$ and all longitudes (180° W to 180° E) with a step of 15° in longitude at model altitude levels corresponding to altitudes of $\sim 60, 50,$ and 41 km . Conversion to the geometrical vertical speed was performed using the hydrostatic equilibrium equation.

It was found that the vertical wind, on average, blows downward in the cold season from October to March and upward in the warm season. In particular, in the period from April to September the vertical wind speed was 1.8 mm/s at a level of 60 km and 0.45 mm/s at 50 km. Averaged over 2014–2016, the vertical wind speed was -0.46 mm/s at an altitude of 60 km and -1.3 mm/s at an altitude of 50 km. Comparison with the abovementioned gravitational sedimentation rates shows that, after averaging over a year, the effect of vertical wind is minor compared to the gravitational sedimentation and only further increases the particle sedimentation rate. The vertical wind will be disregarded in further annual average estimates.

For known G and V_{gravity} , the mass and number concentrations C_M and C_N are determined from the formulas $C_M = G/V_{\text{gravity}}$, $C_N = 3G/(4\pi\langle r^3 \rangle \rho V_{\text{gravity}})$, where ρ is the particle density, $\langle r^3 \rangle$ is the root-mean-cube particle radius. The backscattering coefficients and, correspondingly, the $R(532) - 1$ values in the layer 50–60 km were calculated for a number of meteoric aerosol models [4, 12] and presented in Table 2. For the model nos. 1–4, the refractive indices at a wavelength of 532 nm (first column in Table 2) were $1.635 - 0.005i$ (pyroxene $\text{Mg}_{0.7}\text{Fe}_{0.3}\text{SiO}_3$), $1.706 - 0.045i$ (pyroxene $\text{Mg}_{0.4}\text{Fe}_{0.6}\text{SiO}_3$), $1.61 - 3.8 \times 10^{-5}i$ (weakly absorbing composition), $1.815 - 0.095i$ (olivine $\text{Mg}_{0.8}\text{Fe}_{1.2}\text{SiO}_4$). We assumed that particles were spherical, and that the model-based size distribution was lognormal. The effective radius $r_{32} = \langle r^3 \rangle / \langle r^2 \rangle$, shown in the first row in Table 2, varied in the range from 0.026 to $0.66 \mu\text{m}$, comprising both regions of ultrafine and submicron aerosol particles. The same flux G , corresponding to the global flux 10^4 t/yr , was specified for all models.

Table 2. The $R(532) - 1$ calculations for a number of meteoric aerosol models

Model	r_{32}							
	0.026	0.046	0.066	0.086	0.10	0.26	0.46	0.66
No. 1	0.005	0.013	0.014	0.012	0.0096	0.0096	0.010	0.006
No. 2	0.006	0.015	0.016	0.012	0.0090	0.006	0.003	0.001
No. 3	0.004	0.012	0.014	0.011	0.0093	0.0093	0.011	0.077
No. 4	0.007	0.019	0.019	0.013	0.0089	0.004	0.001	0.0003

From Table 2 it can be seen that the calculated $R(532) - 1$ values approximately correspond to those observed in the periods of elevated backscattering. From the viewpoint of how well it is manifested in backscattering, the r_{32} range from 0.05 to 0.5 μm is most effective for all models. Smaller particles scatter weaker; and larger particles sediment faster and have small concentration. We note that two-wavelength measurements gave an estimate $r_{32} \sim 0.15 \mu\text{m}$ for aerosol layers from the Chelyabinsk meteorite [12].

Comparison of the global flux $\sim 10^4$ t/yr, specified in the calculations, with data in Table 1 indicates that it is much (1.5 orders of magnitude) larger than the fluxes in the region of visible meteors and bolides. It should also be kept in mind that most of the largest meteoroids (bolides) are fragmented at altitudes lower than 50 km [30], not contributing much to the 50–60 km layer. Hence, for about a 1-year period, on average, meteoric aerosol from large meteoroids cannot account for the observed $R(532) - 1$ values. A certain role can be played by interannual and geographic variations in the fluxes; however, they hardly can explain the above-indicated discrepancy of 1.5 orders of magnitude. At the same time, the meteoric material flux in the region of radio meteors (see Table 1), which then form the meteoric smoke, is comparable to the value used in the calculations. This leads us to hypothesize that the observed backscattering is associated just with this group of meteoric materials. The existing models apparently underestimate the possibility for the enlarged fraction of meteoric smoke aerosol particles with sizes 0.05 μm and larger to form in the atmosphere such as due to magnetic dipole interactions [29].

The hypothesis of the enlargement of meteoric smoke particles does not contradict the known SOFIE satellite measurements at a wavelength of 1037 nm [4] and estimates of mass concentration obtained using models of meteoric smoke at an altitude of 55 km [3]. For instance, for model no. 4 with $r_{32} = 0.046 \mu\text{m}$ and $R(532) - 1 = 0.02$, our calculations give the mass concentration $C_M = 3 \times 10^{-16} \text{ g/cm}^3$ and the extinction coefficient $\sigma(1037) = 3.5 \times 10^{-8} \text{ km}$, corresponding closely in order of magnitude to $C_M = (3-8) \times 10^{-16} \text{ g/cm}^3$ derived from simulations [3] and $\sigma(1037) = 5 \times 10^{-8} \text{ km}^{-1}$ typical for SOFIE measurements [4]. The SOFIE observations were reanalyzed recently

using three-wavelength measurements [5]; based on these results, the authors constrained the admissible models to just strongly absorbing compositions, for which the ratio of extinction coefficients $\sigma(330)/\sigma(1037)$ lies in the range 5–10. These models include model no. 4, for which, as our calculations showed, in the chosen size range, the ratio $\sigma(330)/\sigma(1037)$ also lies in the range 5–10. This suggests that SOFIE data are compatible with particle spectra lying both in nanometer and in ultrafine and submicron ranges; as such, these data cannot serve as a sufficient criterion for identifying meteoric smoke particle sizes.

Special attention should be paid to the issue of what atmospheric conditions favored the increase in particle concentration and sizes in late 2015 to early 2016. A few factors favoring their occurrence can be indicated. We primarily note the anomalous vertical wind speed in November 2015, when $R(532) - 1$ rapidly increased: the monthly average vertical wind speed at the 55-km level was -1.1 mm/s , as compared to -6.3 and -7.5 mm/s in 2014 and 2016, respectively. Next, in winter 2015–2016, there were very low stratospheric temperatures in the Arctic and a maximally strong polar stratospheric vortex [31, 32]. Moreover, the polar stratospheric vortex shifted far southward toward Eurasia [33, 34]. The measurements [35] indicate that particle concentration is several-fold higher inside the polar vortex than in extra-vortex areas, with the large particle concentration gradient existing in the region of $\sim 20^\circ$ in latitude relative to the vortex center [36]. Owing to these factors, the meteoric smoke particle concentration might have increased several-fold over the region of lidar measurements in the period of time considered here.

CONCLUSIONS

In this work, we present the lidar measurements of backscattering in the middle atmosphere, performed in the period from 2012 to 2017 in Obninsk (55.1° N , 36.6° E) at wavelengths of 355 and 532 nm. Such long-term and systematic lidar measurements in the middle atmosphere seem to have been carried out for the first time. Also, analogous shorter-lasting measurements in Ardon (43.2° N , 44.3° E) are presented. Averaged over 40–50 and 50–60 km layers, the monthly average $R(532) - 1$, defined as the ratio of

aerosol and Rayleigh backscattering coefficients, vary from 0 to 0.02, while their average peak levels in these layers vary from 0.1 to 0.2. There are short-term (less than 1-month) and long-term (0.5-year and longer) $R(532) - 1$ variations. The short-term variations are correlated in time with the occurrence of certain meteor showers. The long-term $R(532) - 1$ increased in the 50–60 km layer in 2013 after the Chelyabinsk meteorite fall, as well as in the first half of 2016. In 2014–2015, the monthly average $R(532) - 1$ was zero within the measurement error at altitudes from 40 to 60 km.

The results are analyzed assuming the meteoric nature of the aerosol observed. The existing data on the fluxes of different groups of meteoric material and sedimentation rates of meteoric particles are used to estimate the backscattering levels, taking into account the gravitational sedimentation and vertical wind. It is noted that micrometeors and spherules rapidly sediment and, as such, cannot be manifested in backscattering. The visible meteors and bolides can be only responsible for short-term backscattering bursts; however, their fluxes are insufficiently strong to explain long-term (about half-year) backscattering enhancement. The main flux of meteoric material is associated with radio meteors, the ablation products of which are present in the middle atmosphere as meteoric smoke. The enhanced $R(532) - 1$ levels in 2016 can be explained assuming that meteoric smoke particles are enlarged to effective sizes $r_{32} \geq 50$ nm. It is noteworthy that the characteristics of the enlarged fraction still agree with meteoric smoke models in mass concentration and with existing SOFIE satellite measurements in magnitude of scattering coefficients. This can be used to explain both the satellite measurements of extinction and lidar measurements of backscattering. Possible mechanisms of particle enlargement are beyond the scope of this work; we only note that one of the mechanisms could be magnetic-dipole particle interaction. Strengthening of the stratospheric polar vortex and its shift toward Eurasia could seemingly be responsible for the increased concentration of meteoric smoke particles over the region of measurements in winter 2015–2016. On the whole, our interpretation is preliminary in character and could be verified through further studies and, in particular, through continued systematic lidar measurements.

ACKNOWLEDGMENTS

The authors would like to thank T. N. Sykilinde for assistance in the analysis of meteor shower data, as well as the European Centre for Medium-Range Weather Forecasts for providing access to reanalyze data from the ERA-5 project. The paper contains the modified Copernicus Climate Change Service data for 2014–2016.

REFERENCES

1. A. E. Mikirov and V. A. Smerkalov, *The study of scattered radiation of the upper atmosphere of the Earth* (Gidrometeoizdat, Leningrad, 1981) [in Russian].
2. J. M. C. Plane, "Cosmic dust in the Earth's atmosphere," *Chem. Soc. Rev.* **41**, 6507–6518 (2012).
3. C. G. Bardeen, O. B. Toon, E. J. Jensen, D. R. Marsh, and V. L. Harvey, "Numerical simulations of the three-dimensional distribution of meteoric dust in the mesosphere and upper stratosphere," *J. Geophys. Res.* **113**, D17202 (2008).
4. M. E. Hervig, L. L. Gordley, L. E. Deaver, D. E. Siskind, M. H. Stevens, J. M. Russell, III, S. M. Bailey, L. Megner, and C. G. Bardeen, "First satellite observations of meteoric smoke in the middle atmosphere," *Geophys. Res. Lett.* **36**, L18805 (2009).
5. M. E. Hervig, J. S. A. Brooke, W. Feng, C. G. Bardeen, and J. M. C. Plane, "Constraints on meteoric smoke composition and meteoric influx using SOFIE observations with models," *J. Geophys. Res.: Atmos.* **122** (13), 495–505 (2017).
6. V. V. Bychkov and V. N. Marichev, "Formation of water aerosols in the upper stratosphere in periods of anomalous winter absorption of radio waves in the ionosphere," *Atmos. Ocean. Opt.* **21** (3), 219–226 (2008).
7. V. V. Bychkov, B. M. Shevtsov, and V. N. Marichev, "Same statistically average characteristics of occurrence of aerosol scattering in the middle atmosphere of Kamchatka," *Atmos. Ocean. Opt.* **26** (2), 104–106 (2013).
8. V. A. Korshunov, D. S. Zubachev, E. O. Merzlyakov, and Ch. Jacobi, "Aerosol parameters of middle atmosphere measured by two-wavelength lidar sensing and their comparison with radio meteor echo measurements," *Atmos. Ocean. Opt.* **28** (1), 82–88 (2015).
9. A. A. Cheremisin, L. V. Granitskii, V. M. Myasnikov, and N. V. Vetchinkin, "Remote optical sensing in the ultraviolet region of the aerosol layer near the stratopause from onboard the astrophysical space station "Astron"," *Atmos. Ocean. Opt.* **11** (10), 952–957 (1998).
10. P. Keckhut, A. Hauchecorne, and M. L. Chanin, "A critical review of the data base acquired for the long term surveillance of the middle atmosphere by French Rayleigh lidars," *J. Atmos. Ocean. Technol.* **10** (6), 850–867 (1993).
11. A. R. Klekociuk, P. G. Brown, D. W. Pack, D. O. ReVelle, W. N. Edwards, R. E. Spalding, E. Tagliaferri, B. B. Yoo, and J. Zagari, "Meteoritic dust from the atmospheric disintegration of a large meteoroid," *Nature* **436** (7054), 1132–1135 (2005).
12. V. N. Ivanov, D. S. Zubachev, V. A. Korshunov, V. B. Lapshin, M. S. Ivanov, K. A. Galkin, P. A. Gubko, D. L. Antonov, G. F. Tulinov, A. A. Cheremisin, P. V. Novikov, S. V. Nikolashkin, S. V. Titov, and V. N. Marichev, "Lidar observations of stratospheric aerosol traces of Chelyabinsk meteorite," *Opt. Atmos. Okeana* **27** (2), 117–122 (2014).
13. A. A. Cheremisin, P. V. Novikov, I. S. Shnipov, V. V. Bychkov, and B. M. Shevtsov, "Lidar observations and formation mechanism of the structure of stratospheric and mesospheric aerosol layers over

- Kamchatka,” *Geomag. Aeron. (Engl. transl.)* **52** (5), 653–663 (2012).
14. V. I. Gryazin and S. A. Beresnev, “Influence of vertical wind on stratospheric aerosol transport,” *Meteorol. Atmos. Phys.* **110**, 151–162 (2011).
 15. V. Della Corte, J. Franciscus, M. Rietmeijer, Alessandra A. Rotundi, M. Ferrari, and P. Palumbo, “Meteoric CaO and carbon smoke particles collected in the upper stratosphere from an unanticipated source,” *Tellus B: Chem. Phys. Meteorol.* **65** (1), 20174 (2013).
 16. G. N. Glazov, *Statistical Questions of Lidar Sounding of the Atmosphere* (Nauka, Novosibirsk, 1987) [in Russian].
 17. A. Behrendt and T. Nakamura, “Calculation of the calibration constant of polarization lidar and its dependency on atmospheric temperature,” *Opt. Express* **10** (16), 805–817 (2002).
 18. M. Adam, “Notes on temperature-dependent lidar equations,” *J. Atmos. Ocean. Technol.* **26** (6), 1021–1039 (2009).
 19. F. J. M. Rietmeijer, “Interrelationships among meteoric metals, meteors, interplanetary dust, micrometeorites, and meteorites,” *Meteorit. Planet. Sci.* **35** (5), 1025–1041 (2000).
 20. P. Spurny, J. Borovicka, H. Mucke, and J. Svoren, “Discovery of a new branch of the Taurid meteoroid stream as a real source of potentially hazardous bodies,” *Astron. Astrophys.* **605**, A68 (2017).
 21. International Meteor Organization. Visual Meteor Database. https://www.imo.net/members/imo_vmdb/ (Cited March 5, 2018).
 22. R. R. Neely, III, J. M. English, O. B. Toon, S. Solomon, M. Mills, and J. P. Thayer, “Implications of extinction due to meteoritic smoke in the upper stratosphere,” *Geophys. Res. Lett.* **38**, L24808 (2011). doi 10.1029/2011GL049865
 23. Z. Ceplecha, J. Borovicka, W. Elford, D. Revelle, R. Hawkes, V. Porubcan, and M. Simek, “Meteor phenomena and bodies,” *Space Sci. Rev.* **84** (3/4), 327–471 (1998).
 24. J. D. Carrillo-Sanchez, J. M. C. Plane, W. Feng, D. Nesvorny, and D. Janches, “On the size and velocity distribution of cosmic dust particles entering the atmosphere,” *Geophys. Res. Lett.* **42** (15), 6518–6525 (2015). doi 10.1002/2015GL065149
 25. O. Kalashnikova, M. Horanyi, G. E. Thomas, and O. B. Toon, “Meteoric smoke production in the atmosphere,” *Geophys. Res. Lett.* **27** (20), 3293–3296 (2000).
 26. P. Brown, R. E. Spalding, D. ReVelle, O. E. Tagliaferri, and S. P. Worden, “The flux of small near-Earth objects colliding with the Earth,” *Nature* **420**, 314–316 (2002).
 27. V. A. Filippov, Candidate’s Dissertation in Mathematics and Physics (Joint-Stock Company “National Center of Space Research and Technology”, Almaty, 2010).
 28. V. I. Gryazin and S. A. Beresnev, “About vertical motion of fractal-like particles in the atmosphere,” *Opt. Atmos. Okeana* **24** (6), 506–509 (2011).
 29. R. W. Saunders, S. Dhomse, W. S. Tian, M. P. Chipperfield, and J. M. C. Plane, “Interactions of meteoric smoke particles with sulphuric acid in the Earth’s stratosphere,” *Atmos. Chem. Phys.* **12**, 4387–4398 (2012).
 30. Jet propulsion laboratory. Fireball and Bolide Data. <https://www.cneos.jpl.nasa.gov/fireballs/> (Cited April 10, 2018).
 31. V. Matthias, A. Dornbrack, and G. Stober, “The extraordinary strong and cold polar vortex in the early northern winter 2015/2016,” *Geophys. Res. Lett.* **43** (23), 12.287–12.294 (2016).
 32. F. M. Palmeiro, M. Iza, D. Barriopedro, N. Calvo, and R. Garcia-Herrera, “The complex behavior of El Nino winter 2015–2016,” *Geophys. Res. Lett.* **44** (6), 2902–2910 (2017).
 33. M. P. Nikiforova, A. M. Zvyagintsev, P. N. Vargin, N. S. Ivanova, A. N. Lukyanov, and I. N. Kuznetsova, “Anomalously low total ozone levels over the Northern Urals and Siberia in late January 2016,” *Atmos. Ocean. Opt.* **30** (3), 255–262 (2017).
 34. E. P. Kropotkina, S. V. Solomonov, S. B. Rozanov, A. N. Ignat’ev, and A. N. Lukin, “Variations in the Ozone concentration in the stratosphere over Moscow due to dynamic processes in the cold period of 2015–2016,” *Bull. Lebedev Phys. Inst.* **45** (1), 19–23 (2018).
 35. J. Curtius, R. Weigel, H.-J. Vossing, H. Wernli, A. Werner, C.-M. Volk, P. Konopka, M. Krebsbach, C. Schiller, A. Roiger, H. Schlager, V. Dreiling, and S. Borrmann, “Observations of meteoric material and implications for aerosol nucleation in the winter Arctic lower stratosphere derived from in situ particle measurements,” *Atmos. Chem. Phys.* **5** (11), 3053–3069 (2005).
 36. L. Megner, D. E. Siskind, M. Rapp, and J. Gumbel, “Global and temporal distribution of meteoric smoke: A two dimensional simulation study,” *J. Geophys. Res.* **113**, D03202 (2008). doi 10.1029/2007JD009054

Translated by O. Bazhenov